UCSF
UC San Francisco Electronic Theses and Dissertations

Title
Developing Methods to Aid Edge Detection in a Micro-Computed Tomography Based Subcutaneous Versus Visceral Fat Segmentation Algorithm

Permalink
https://escholarship.org/uc/item/999656wt

Author
Shetty, Charvi

Publication Date
2013

Peer reviewed|Thesis/dissertation

eScholarship.org Powered by the California Digital Library
University of California

Developing Methods to Aid Edge Detection in a Micro-Computed Tomography Based Subcutaneous Versus Visceral Fat Segmentation Algorithm

by

Charvi Shetty

THESIS

Submitted in partial satisfaction of the requirements for the degree of

MASTER OF SCIENCE

in

Biomedical Imaging

in the

GRADUATE DIVISION

of the

UNIVERSITY OF CALIFORNIA, SAN FRANCISCO

Acknowledgements

I would like to thank Dr. Richard Carano for his guidance during the course of this work and serving as an excellent mentor during my stay at Genentech. I am also grateful for having him and Kai Barck being patient enough to teach me how to write code in C, a programming language I had to pick up quickly in order to develop the algorithm to complete this work. This project would not have been possible without Shelby Wyatt, who has continuously offered her assistance in helping in any way possible and for making edits to the earlier drafts of this paper, along with Dr. Carano.

I would also like to thank my thesis committee at UCSF, especially my committee chair, Dr. Alastair Martin, for facilitating the project in collaboration with industry. It has been a great pleasure working with Dr. Mark Wilson and Dr. Thomas Lang for their advice and encouragement.

Last but certainly not the least, I would like to thank Dr. Pratik Mukherjee for his continued guidance and training, as it has been an extreme pleasure working with him for the past couple of years, and I couldn't be in the position I am in right now without his help. Words alone cannot capture the gratitude I have for his efforts and invaluable advice.

I am also truly grateful for my family and friends who have morally supported me throughout this work, and for always believing in me.

Developing Methods to Aid Edge Detection in a Micro-Computed Tomography Based Subcutaneous Versus Visceral Fat Segmentation Algorithm

Charvi Shetty

Abstract

Micro-computed tomography can be used to provide a precise in-vivo assessment of adipose tissue quantity and distribution, including information on subcutaneous and visceral fat volume in mouse models. This study aims to develop methods to aid edge detection in order to eventually segment out the visceral and subcutaneous fat compartments automatically. The algorithm detailed in this paper optimizes steps in the Canny edge detection method and utilizes low-pass filtering and gradient edge detection. Ten mice (weight range: 19.96 – 57.66 g) were tested with micro-CT scans to verify the utility of this algorithm. The algorithm demonstrated stability despite the broad range of body weights and adiposity. Comparisons of the data between unfiltered versus filtered mice volumes suggest that this algorithm can be used to effectively increase edge strength for use in separating visceral and subcutaneous fat compartments. The eventual application of this method would be to assess metabolic disease risk, such as those associated with central obesity including diabetes, hypertension, and heart disease.

TABLE OF CONTENTS

LIST OF FIGURES

LIST OF TABLES

Introduction

The prevalence of obesity has been increasing in recent years, which has been associated with increased risk for diabetes, hypertension and heart disease. Moreover, health risk is associated with the location as well as amount of fat, with fat being situated in areas of the body such as under the epidermis and around vital organs[1]. Fat distribution varies greatly with gender, genetic background, age, disease state, and response to drugs and hormones. Fat stored closer to the skin is categorized as subcutaneous fat, whereas fat surrounding organs is part of the visceral fat compartment. Central obesity has a higher health risk associated with metabolic syndrome as opposed to peripheral obesity. Clinically, x-ray based computed tomography (CT) is one of the methods used to observe fat deposition, with other technologies including magnetic resonance imaging (MRI), dual energy x-ray absorptiometry (DEXA) and quantitative nuclear magnetic resonance (QMR)[2,3]. Micro-MRI has been used successfully to phenotype mouse models of obesity but the technology is not readily available to most researchers, and although DEXA and QMR based scanning effectively characterizes lean and fat volumes in mice, they do not provide detailed spatial information on fat distribution. It is known that animal models can model human diseases associated with visceral fat, and that in-vivo micro-CT can provide spatial information of fat distribution in mice[4,5].

An image segmentation algorithm that was previously developed at Genentech included a fully automated method to segment out lean mass, adipose tissue and bone from micro-CT mice volumes[5]. Micro-CT has the advantage of being a truly quantitative method, as different tissue types have defined ranges in Hounsfield Units (HU). Fat is in the lower range of -190 to -30 HU, lean mass in the middle range from -29 to 150 HU, and bone is in a higher range of greater than 400 HU[6,7]. Therefore, the Wyatt et al. algorithm takes

advantage of thresholding and morphological filtering to obtain each of the main body compartments. Three masks are generated from this algorithm, as can be seen in Figure 1 with the axial view of the original micro-CT mouse volume (a), the whole body volume (b), adipose tissue (c), and bone masks (d). A significant improvement of this algorithm would be to automatically sub-divide the visceral and subcutaneous fat compartments of the adipose tissue.

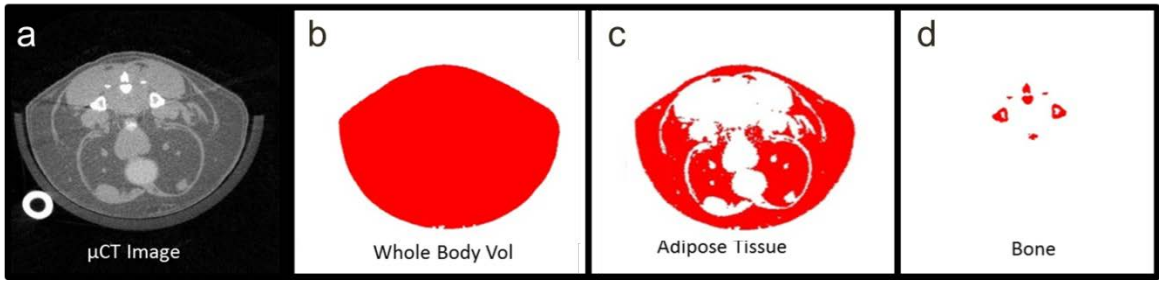

Figure 1. a) Original micro-CT mouse volume, b) whole body mask, c) adipose tissue mask, and d) bone mask generated by the Shelby et al. algorithm[7].

The primary demarcation line used to separate the visceral and subcutaneous fat compartments is the abdominal wall lining. In a density based micro-CT volume, the abdominal wall layer appears brighter than the surrounding fat tissue due to its higher density. A recent algorithm has been introduced that segments the total abdominal adiposity into visceral and subcutaneous fat compartments[5]. Figure 2 displays the 3D rendering of the micro-CT data of subcutaneous fat in yellow and visceral fat in red, in both the sagittal and coronal views of the mouse. The abdominal wall lining is the dark line separating the visceral (red) and subcutaneous (yellow) fat compartments in the coronal view. This thesis work focuses on improving on the algorithm described in Lublinsky et al., which will be described in detail in the later sections.

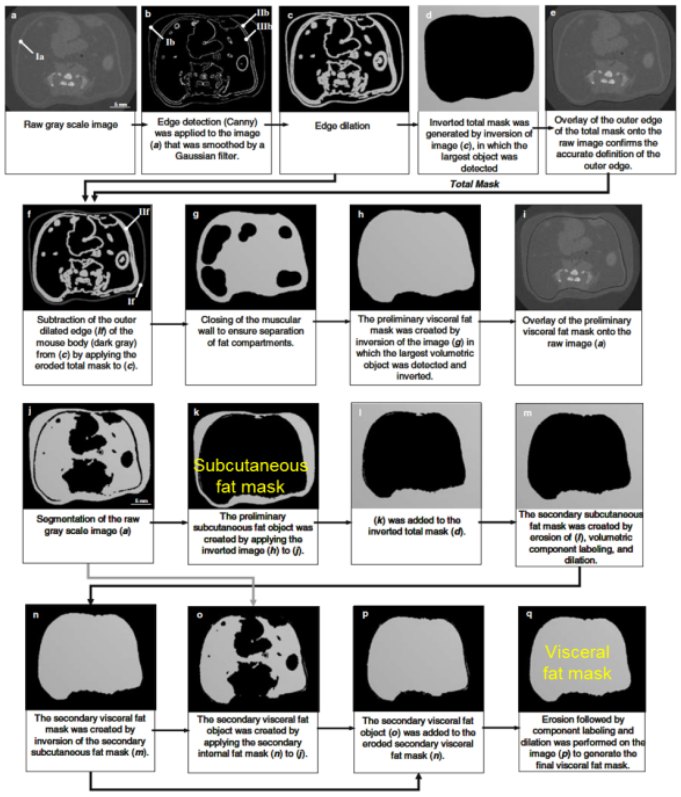

Figure 2 (top). Sagittal and coronal views of a micro-CT 3D rendering of a mouse, showing the subcutaneous fat compartment (red) and visceral fat compartment (yellow) separated by the abdominal wall lining[5].

Figure 3 (right). Lublinsky et al. implementation of visceral versus subcutaneous fat compartment segmentation[5].

As mentioned previously, proper identification of the abdominal wall is crucial for segmenting out the two different fat compartments, and so this study aims to optimize the edge detection algorithm used in the Lublinsky paper. Once the abdominal wall boundary is properly detected, as in Figure 3, morphological filtering and filling will be performed to segment the subcutaneous and visceral fat. Nevertheless, the identification of the abdominal wall boundary is critical, as the steps following this are largely straight-forward. The major limitation of the Lublinsky paper is that it is not fully automated in regards to the slice selection in the abdominal region for the compartmentalization, as the definition for the abdominal volume was manually restricted to the region between L1 and L5 vertebrae. Limiting the abdominal volume of interest might cause inaccuracies in

discriminating visceral and subcutaneous fat, especially in lean mice, in which the total volume of evaluated fat deposits would be greatly reduced[3]. The objective of this thesis is to fully automate the slice selection process so that the algorithm can capture the entire abdominal region in a standardized way, permitting it to be efficiently applied to thousands of CT volumes, including both lean and fat mice, for later studies.

The performance criteria for the Canny edge detection includes minimizing the probability of failing to detect real edge points, minimizing the probability of falsely marking non-edge points, points marked as edge points being as close as possible to the center of the true edge, and having only one response to a single edge[8]. The Canny edge detection method was used in Lublinsky's paper to isolate the abdominal wall, with the goal of my thesis being the refinement and optimization of the approach. The Canny edge detector is an algorithm optimized for finding step edges in the presence of noise, and consists of 5 major steps[9]. This study focuses on the first 2 steps, which includes the low-pass filtering step and gradient edge detection. The low-pass filtering step serves to smooth the image in order to reduce noise and the gradient detection step marks where the gradients of the image have large magnitudes, such as through the application of the Sobel operator. The remaining Canny steps consist of non-maximum suppression, double thresholding and edge tracking by hysteresis, which will be implemented during the rest of my stay at Genentech. The non-maximum suppression step marks only the local maxima as edges, double thresholding determines potential edges by marking pixels stronger than the high threshold as strong and those weaker than the low threshold as weak, and the edge tracking by hysteresis determines final edges by suppressing all edges that are not connected to a very strong edge.

Materials and Methods

A TriFoil Imaging eXplore CT120 (Northridge, CA) micro-CT scanner was used to image mice in-vivo in the prone position from the tip of the nose to the base of the tail with a 70kV tube voltage, 40mA tube current, 4x4 detector bin mode, 20ms exposure time, 100 µm voxel size, 0 gain and 900 views at an approximately 10 minute scan time for four mice. All animal procedures were approved by Genentech's Institutional Animal Care and Use Committee. Two groups of mice from the The Jackson Laboratory (Bar Harbor, ME) were imaged with microCT: (1) C57BL/6J male mice which have been fed a high fat (60 kcal%) diet starting at six weeks of age (diet-induced obesity mice, DIO) and (2) control B6 males fed a 10 kcal% diet containing the same protein content as the high fat diet. For the duration of the micro-CT imaging, mice were slightly anesthetized with approximately two percent isoflurane in medical air and body temperature was maintained at 37ºC using warm airflows. As can be seen in Figure 4, four mice can be scanned at a time with our setup, and scans can be completed within 10 minutes for a high throughput. The resulting axial slice CT images showing the abdominal region of each of the four mice is shown in Figure 4b.

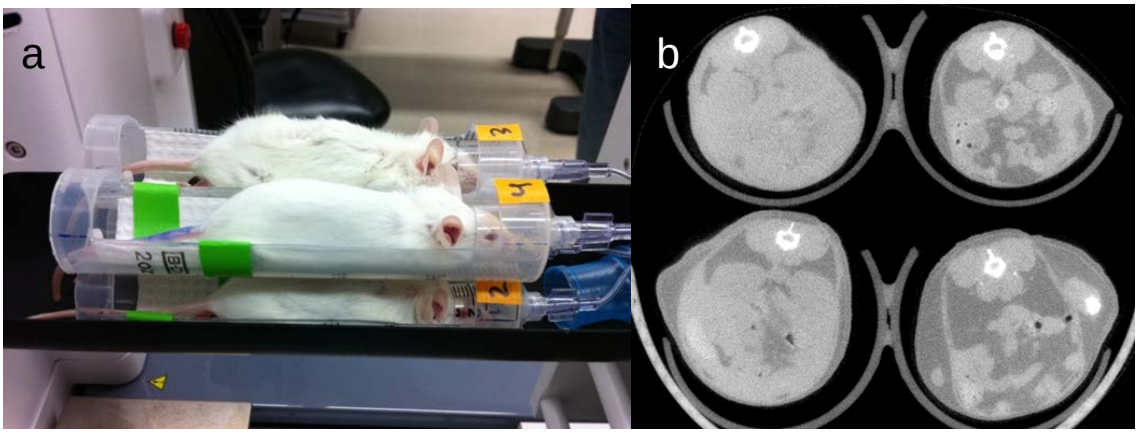

Figure 4. a) Four-mouse holder for micro-CT scanning and b) resulting axial slice CT images of the abdominal region.

All image analysis algorithms were developed using the C++ programming language and AVW function libraries (AnalyzeDirect, Overland Park, KS). Prior to analysis, the micro-CT image *.isq files were converted to the required AVW volume data format. The subcutaneous and visceral fat analysis employed a whole-body mask (WBM) generated by a fully-automated body composition algorithm (Wyatt et al, unpublished). The WBM was generated by employing image intensity thresholding and morphological filtering. A threshold was applied to segment objects in the image from air. The mouse body was initially segmented from the micro-CT platform, anesthesia tube and noise using an intensity threshold followed by the application of three morphological filtering steps: open (3x3x1), fill, and erode (5x5x1). A connectivity algorithm, AVW_FindVolumeComponents, sorted and labeled objects with a connectivity of 6 (AVW_6_CONNECTED), where the largest object is assigned to the WBM (volume and object).

Three low-pass filters, the adaptive restoration, median, and Gaussian, were individually applied onto the CT volumes using the Analyze toolkit coded in C. The adaptive restoration and median filters were evaluated using various 2D kernels of sizes including 3x3, 5x5, 7x7, 9x9, 11x11 and 21x21. Gaussian smoothing was implemented with variances of 1, 4, 9, 16 and 25. After inspecting the 2D filtering results visually and quantitatively through region of interest (ROI) analysis, the median filter was then expanded to the third dimension. For each data set, two ROIs were manually defined across three slices within the abdominal area, located 50 slices apart from each other. The ROI values were then averaged across the three slices to calculate the contrast-to-noise

ratio in ten mice, consisting of four lean, two mid-sized, and four obese mice with corresponding weights described in Table 1.

Mouse Number	1086_1	1089_4	2710_1	2712_1	1087_2	1088_4	1090_3	1087_3	1088_1	1089_1
Weight (g)	24.58	24.61	20.17	19.96	35.12	34.21	57.66	55.18	54.4	52.66
Mouse Type	Lean	Lean	Lean	Lean	Mid	Mid	Fat	Fat	Fat	Fat

Table 1. Mouse numbers and corresponding weights for mouse type categorization.

The three non-linear smoothing filters were the adaptive restoration (ADR), median and Gaussian filters. The ADR filter is a low-pass filter that operates on an intensity image degraded by constant power additive noise using a pixel-wise adaptive method based on local neighborhood statistics[10]. A median filter is a nonlinear filter that removes impulse noise yet preserves edges and consists of a sliding window encompassing an odd number of pixels. The center pixel in the window is replaced by the median of the pixels in the window[11]. The median filter is useful for removing isolated lines or pixels while preserving spatial resolution. A Gaussian filter is a linear low-pass filter that results in the blurring of an image to reduce image noise through the convolution of a Gaussian function with a defined variance. The employed variance was the square of the Gaussian distribution standard deviation.

For each mouse, two sets of ROIs were generated on a slice. One ROI was manually placed on the abdominal wall (red circle in Figure 5) and the other ROI was drawn in the fat region (green circle in Figure 5). The difference in mean intensities of the two regions was then divided by the standard deviation of the ROI drawn in the fat region to calculate the CNR, as can be seen in the equation below. The same approach was applied to a second set of ROIs drawn on the opposite side of the mouse (yellow circle on abdominal wall and blue circle in the fat region), and this ROI generation method was performed

across a total of three different slices within the abdominal region, located 50 slices away from each other. The start slice (Slice 1) was chosen to be at the base of the kidney, as marked through manual visual inspection, with Slice 2 being 50 slices away on the raw CT volume from Slice 1, and Slice 3 being 100 slices superior to Slice 1.

$$\text{Contrast-to-noise ratio} = \frac{\text{Mean of Region 1} - \text{Mean of Region 2}}{\text{Standard Deviation of Region 2}}$$

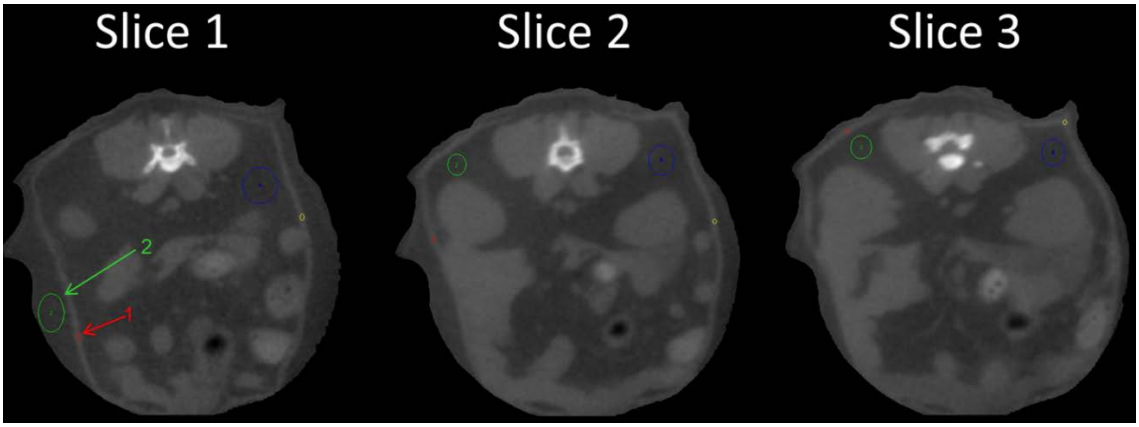

Figure 5. ROI placement for CNR calculations using Region 1 (red) on abdominal wall and Region 2 (green) in the fat region shown across three slices.

Results

The adaptive restoration filter results on axial slices are displayed in Figure 6, qualitatively showing increased levels of smoothing and blurring of edges with increasing kernel sizes. Quantitative results of the ADR filter at various kernel sizes across all mice are presented in Table 2.

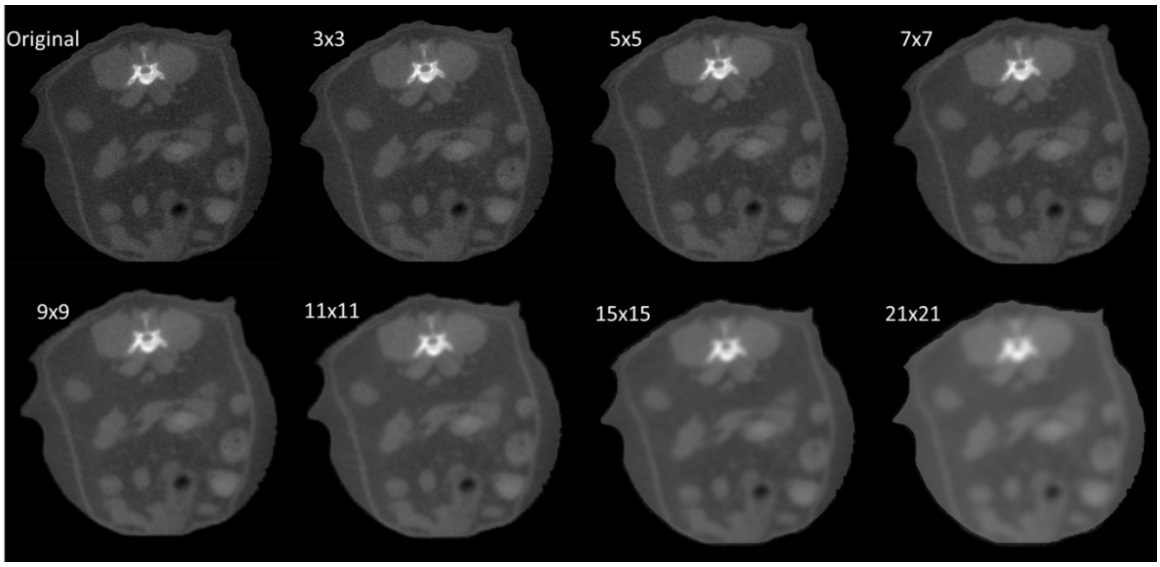

Figure 6. Adaptive restoration filter performed across 2D kernel sizes including 3x3, 5x5, 7x7, 9x9, 11x11, 15x15 and 21x21.

Table 2. Adaptive restoration filter mean CNR results averaged across three slices for individual mice.

Mouse Type	Mouse Number	Kernel Size	Mean CNR	Mouse Type	Mouse Number	Kernel Size	Mean CNR
Lean mouse	1086_1	3	4.77	Mid Mouse	1088_4	3	7.33
Lean mouse	1086_1	5	6.53	Mid Mouse	1088_4	5	9.88
Lean mouse	1086_1	7	8.23	Mid Mouse	1088_4	7	13.54
Lean mouse	1086_1	9	8.91	Mid Mouse	1088_4	9	17.49
Lean mouse	1086_1	11	9.58	Mid Mouse	1088_4	11	20.52
Lean mouse	1086_1	15	9.71	Mid Mouse	1088_4	15	24.08
Lean mouse	1086_1	21	8.37	Mid Mouse	1088_4	21	22.52
Lean mouse	1089_4	3	4.49	Fat Mouse	1090_3	3	6.72
Lean mouse	1089_4	5	5.65	Fat Mouse	1090_3	5	8.49
Lean mouse	1089_4	7	7.08	Fat Mouse	1090_3	7	10.35
Lean mouse	1089_4	9	8.44	Fat Mouse	1090_3	9	11.77
Lean mouse	1089_4	11	9.51	Fat Mouse	1090_3	11	12.78
Lean mouse	1089_4	15	11.17	Fat Mouse	1090_3	15	13.85
Lean mouse	1089_4	21	11.06	Fat Mouse	1090_3	21	13.42
Lean mouse	2710_1	3	3.91	Fat Mouse	1087_3	3	8.14
Lean mouse	2710_1	5	4.95	Fat Mouse	1087_3	5	10.60
Lean mouse	2710_1	7	5.65	Fat Mouse	1087_3	7	13.33
Lean mouse	2710_1	9	5.76	Fat Mouse	1087_3	9	15.42
Lean mouse	2710_1	11	5.19	Fat Mouse	1087_3	11	16.77
Lean mouse	2710_1	15	3.96	Fat Mouse	1087_3	15	17.67
Lean mouse	2710_1	21	2.44	Fat Mouse	1087_3	21	15.11
Lean mouse	2712_1	3	0.58	Fat Mouse	1088_1	3	6.48
Lean mouse	2712_1	5	0.53	Fat Mouse	1088_1	5	8.64
Lean mouse	2712_1	7	0.82	Fat Mouse	1088_1	7	11.13

Lean mouse	2712_1	9	1.80	Fat Mouse	1088_1	9	13.20
Lean mouse	2712_1	11	2.24	Fat Mouse	1088_1	11	14.70
Lean mouse	2712_1	15	1.03	Fat Mouse	1088_1	15	15.86
Lean mouse	2712_1	21	-3.24	Fat Mouse	1088_1	21	14.91
Mid Mouse	1087_2	3	6.83	Fat Mouse	1089_1	3	6.04
Mid Mouse	1087_2	5	8.62	Fat Mouse	1089_1	5	7.87
Mid Mouse	1087_2	7	10.60	Fat Mouse	1089_1	7	10.02
Mid Mouse	1087_2	9	12.62	Fat Mouse	1089_1	9	11.77
Mid Mouse	1087_2	11	14.46	Fat Mouse	1089_1	11	12.69
Mid Mouse	1087_2	15	16.93	Fat Mouse	1089_1	15	12.47
Mid Mouse	1087_2	21	16.24	Fat Mouse	1089_1	21	10.83

The median filter results are shown in Figure 7, demonstrating increased smoothing with increased kernel size, yet still preserving crisp edges even at the larger kernel sizes. This can be appreciated on the image where kernel sizes of 15x15 and 21x21 are employed. The largest kernel size was restricted to 21x21 because the thickness of the abdominal wall at its thinnest point was 11 pixels wide. The size of the kernel should not exceed double the size of the feature of interest. Quantitative median filter results at various kernel sizes across all mice can be seen in Table 2.

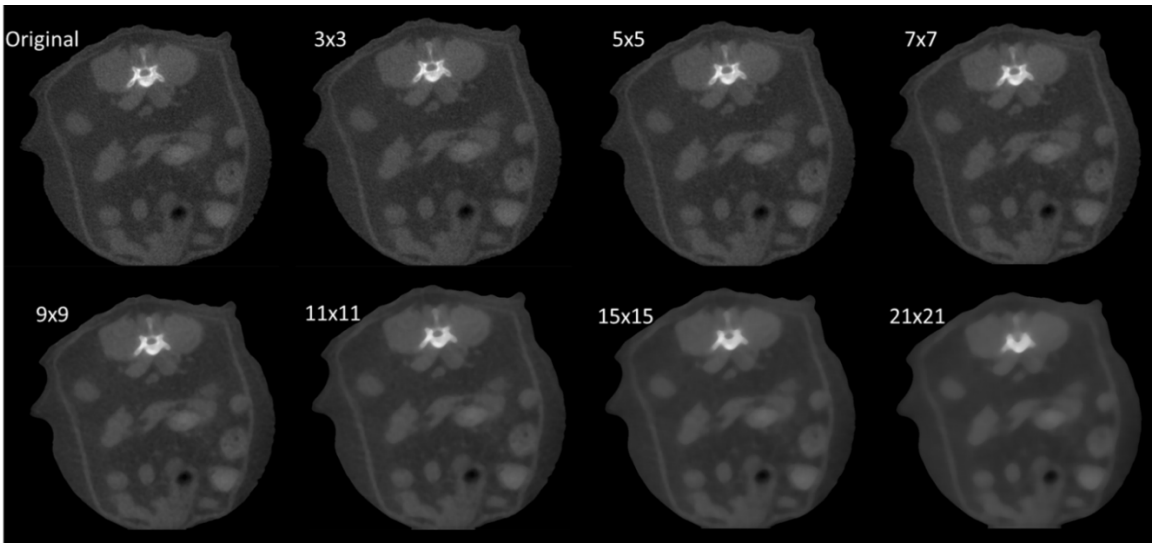

Figure 7. Median filter results across 2D kernel sizes including 3x3, 5x5, 7x7, 9x9, 11x11, 15x15 and 21x21.

Table 3. 2D Median filter mean CNR results averaged across three slices for individual mice.

Mouse Type	Mouse Number	Kernel Size	Mean CNR	Mouse Type	Mouse Number	Kernel Size	Mean CNR
Lean mouse	1086_1	3	4.44	Mid mouse	1088_4	3	6.94
Lean mouse	1086_1	5	5.93	Mid mouse	1088_4	5	9.08
Lean mouse	1086_1	7	7.31	Mid mouse	1088_4	7	12.03
Lean mouse	1086_1	9	8.14	Mid mouse	1088_4	9	14.98
Lean mouse	1086_1	11	9.13	Mid mouse	1088_4	11	17.84
Lean mouse	1086_1	15	11.86	Mid mouse	1088_4	15	22.59
Lean mouse	1086_1	21	12.54	Mid mouse	1088_4	21	26.49
Lean mouse	1089_4	3	4.49	Fat Mouse	1090_3	3	6.52
Lean mouse	1089_4	5	5.77	Fat Mouse	1090_3	5	8.16
Lean mouse	1089_4	7	7.37	Fat Mouse	1090_3	7	9.95
Lean mouse	1089_4	9	8.99	Fat Mouse	1090_3	9	11.52
Lean mouse	1089_4	11	10.16	Fat Mouse	1090_3	11	12.85
Lean mouse	1089_4	15	11.76	Fat Mouse	1090_3	15	14.42
Lean mouse	1089_4	21	13.89	Fat Mouse	1090_3	21	14.50
Lean mouse	2710_1	3	3.78	Fat Mouse	1087_3	3	7.89
Lean mouse	2710_1	5	4.69	Fat Mouse	1087_3	5	10.06
Lean mouse	2710_1	7	5.52	Fat Mouse	1087_3	7	12.67
Lean mouse	2710_1	9	6.17	Fat Mouse	1087_3	9	14.86
Lean mouse	2710_1	11	6.56	Fat Mouse	1087_3	11	16.63
Lean mouse	2710_1	15	6.14	Fat Mouse	1087_3	15	19.13
Lean mouse	2710_1	21	4.86	Fat Mouse	1087_3	21	19.22
Lean mouse	2712_1	3	0.67	Fat Mouse	1088_1	3	6.28
Lean mouse	2712_1	5	0.84	Fat Mouse	1088_1	5	8.25
Lean mouse	2712_1	7	1.17	Fat Mouse	1088_1	7	10.61
Lean mouse	2712_1	9	2.06	Fat Mouse	1088_1	9	12.92
Lean mouse	2712_1	11	2.47	Fat Mouse	1088_1	11	14.88
Lean mouse	2712_1	15	3.16	Fat Mouse	1088_1	15	16.76
Lean mouse	2712_1	21	-0.14	Fat Mouse	1088_1	21	14.66
Mid mouse	1087_2	3	6.54	Fat Mouse	1089_1	3	5.85
Mid mouse	1087_2	5	8.16	Fat Mouse	1089_1	5	7.52
Mid mouse	1087_2	7	10.19	Fat Mouse	1089_1	7	9.72
Mid mouse	1087_2	9	12.19	Fat Mouse	1089_1	9	11.87
Mid mouse	1087_2	11	14.01	Fat Mouse	1089_1	11	13.22
Mid mouse	1087_2	15	17.69	Fat Mouse	1089_1	15	13.41
Mid mouse	1087_2	21	17.81	Fat Mouse	1089_1	21	11.07

Gaussian smoothing results are shown in Figure 8, with increased levels of smoothing with increased variance. Noise from the background seems to be reduced at larger variances, as opposed to the Gaussian with a variance of 1. Streaks and noise are reduced,

but small objects and thin layers are blurred out. Quantitative Gaussian filter results can be seen in Table 3.

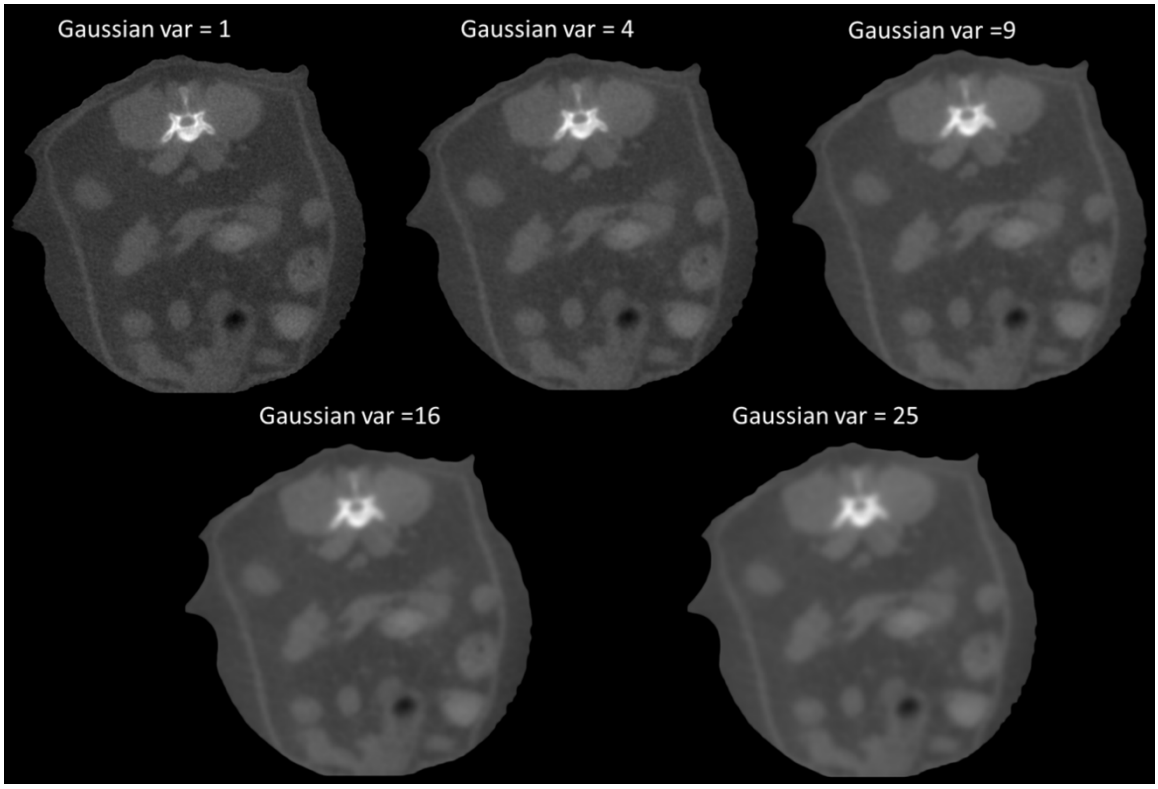

Figure 8. Discrete Gaussian filter applied across variances of 1, 4, 9, 16 and 25.

Table 4. Discrete Gaussian filter mean CNR results averaged across three slices for individual mice.

Mouse Type	Mouse Number	Gaussian Variance	Mean CNR	Mouse Type	Mouse Number	Gaussian Variance	Mean CNR
Lean	1086_1	1	5.10	Mid	1088_4	1	7.84
Lean	1086_1	4	7.58	Mid	1088_4	4	12.57
Lean	1086_1	9	9.14	Mid	1088_4	9	18.69
Lean	1086_1	16	9.854	Mid	1088_4	16	23.85
Lean	1086_1	25	9.75	Mid	1088_4	25	26.56
Lean	1089_4	1	4.85	Fat	1090_3	1	7.18
Lean	1089_4	4	6.75	Fat	1090_3	4	9.98
Lean	1089_4	9	8.71	Fat	1090_3	9	12.24
Lean	1089_4	16	10.371	Fat	1090_3	16	13.56
Lean	1089_4	25	11.67	Fat	1090_3	25	14.13
Lean	2710_1	1	4.15	Fat	1087_3	1	8.72
Lean	2710_1	4	5.54	Fat	1087_3	4	12.71
Lean	2710_1	9	4.97	Fat	1087_3	9	16.16
Lean	2710_1	16	3.59	Fat	1087_3	16	17.61
Lean	2710_1	25	2.68	Fat	1087_3	25	17.52

Lean	2712_1	1	0.62	Fat	1088_1	1	6.99
Lean	2712_1	4	0.57	Fat	1088_1	4	10.55
Lean	2712_1	9	1.06	Fat	1088_1	9	13.96
Lean	2712_1	16	-0.79	Fat	1088_1	16	16.04
Lean	2712_1	25	-3.02	Fat	1088_1	25	16.76
Mid	1087_2	1	7.22	Fat	1089_1	1	6.48
Mid	1087_2	4	10.19	Fat	1089_1	4	9.45
Mid	1087_2	9	13.38	Fat	1089_1	9	12.10
Mid	1087_2	16	16.08	Fat	1089_1	16	13.32
Mid	1087_2	25	17.65	Fat	1089_1	25	13.38

Statistics was performed using a 2-tailed, paired t-test for ten mice, showing a significant increase in CNR for the ADR and median filter at kernel sizes of 7x7 and larger, and at variances of greater than 4 for the Gaussian implementation, as can be seen in Figure 9. At larger kernel sizes for ADR and higher variances for the Gaussian filter implementation, the outer boundary of the mice seems to be degraded, whereas the median filter keeps the outer boundary intact. The demonstrated preservation of edges motivated a 3D implementation of the median kernel.

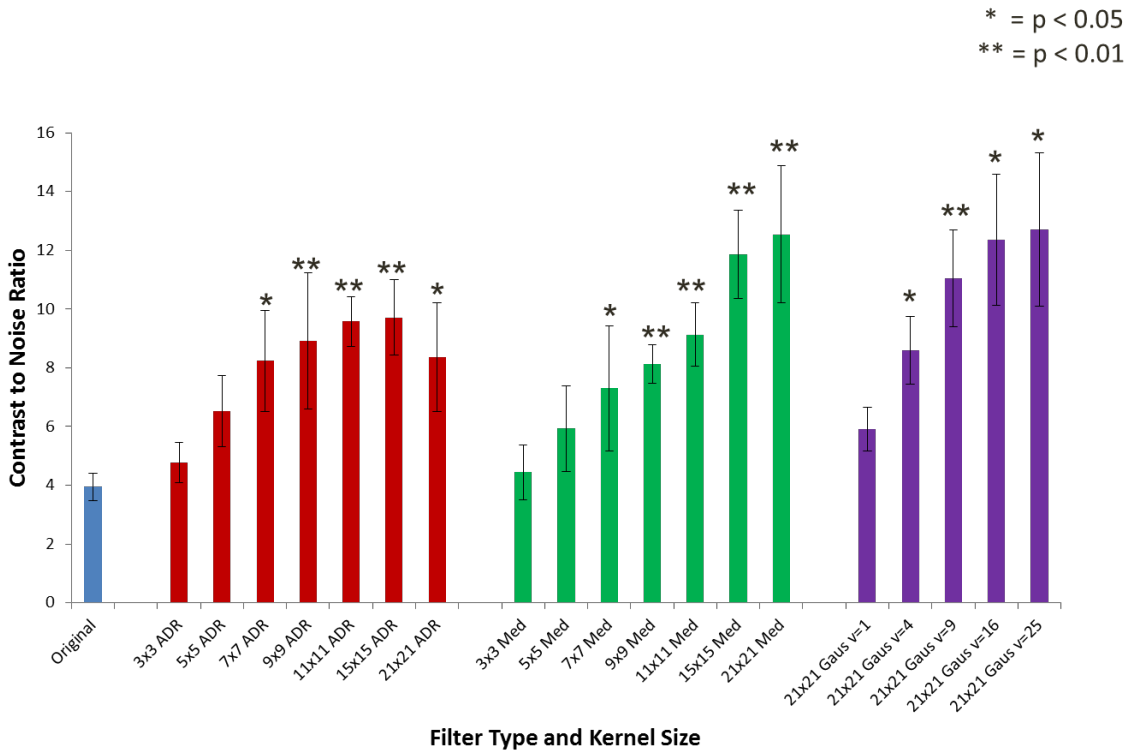

Figure 9. Mean CNR results across various low-pass filtering methods.

The 3D median filter results are shown in Figure 10 with various depths of z = 3, 5, 11, and 21. It can be observed that the abdominal wall thickness increases with increasing depth of the kernel. The quantitative performance of the 3D median filter is noted in Table 5.

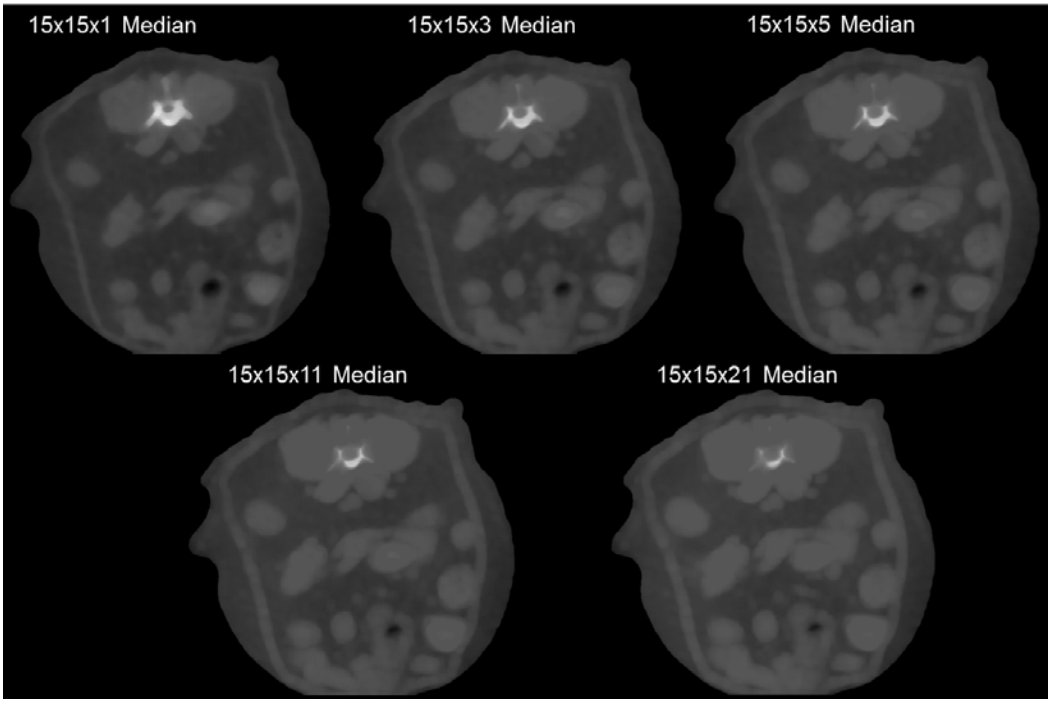

Figure 10. 3D Median filter applied across 15x15 Median smoothed images at depths of 1, 3, 5, 11, and 21.

Table 5. 3D median filter results for individual mice for 15x15 median kernels of depths 1, 3, 5, 11 and 21.

Mouse Type	Mouse Number	Kernel Depth	Slice Mean	Mouse Type	Mouse Number	Kernel Depth	Slice Mean
Lean Mouse	1086_1	3z	12.18	Mid Mouse	1088_4	3z	22.88
Lean Mouse	1086_1	5z	10.89	Mid Mouse	1088_4	5z	23.58
Lean Mouse	1086_1	11z	10.37	Mid Mouse	1088_4	11z	21.76
Lean Mouse	1086_1	21z	11.56	Mid Mouse	1088_4	21z	23.33
Lean Mouse	1089_4	3z	12.04	Fat Mouse	1090_3	3z	14.06
Lean Mouse	1089_4	5z	11.40	Fat Mouse	1090_3	5z	14.04
Lean Mouse	1089_4	11z	10.70	Fat Mouse	1090_3	11z	14.14
Lean Mouse	1089_4	21z	10.41	Fat Mouse	1090_3	21z	14.49
Lean Mouse	2710_1	3z	5.96	Fat Mouse	1087_3	3z	19.79
Lean Mouse	2710_1	5z	6.84	Fat Mouse	1087_3	5z	20.56
Lean Mouse	2710_1	11z	7.69	Fat Mouse	1087_3	11z	22.23

Lean Mouse	2710_1	21z	7.55	Fat Mouse	1087_3	21z	23.61
Lean Mouse	2712_1	3z	2.54	Fat Mouse	1088_1	3z	17.38
Lean Mouse	2712_1	5z	1.08	Fat Mouse	1088_1	5z	17.63
Lean Mouse	2712_1	11z	1.15	Fat Mouse	1088_1	11z	18.39
Lean Mouse	2712_1	21z	0.82	Fat Mouse	1088_1	21z	18.49
Mid Mouse	1087_2	3z	18.83	Fat Mouse	1089_1	3z	13.69
Mid Mouse	1087_2	5z	18.55	Fat Mouse	1089_1	5z	14.99
Mid Mouse	1087_2	11z	18.78	Fat Mouse	1089_1	11z	15.85
Mid Mouse	1087_2	21z	21.19	Fat Mouse	1089_1	21z	15.82

Figure 11 contains the same graph from a previous section, with the addition of the 3D median filter results, which perform similarly with 2D 15x15 and 21x21 Median filters. Therefore, we chose to move forward with the best performing filtered image results based on CNR and general image appearance, for the next step of the segmentation algorithm, which is the application of the Sobel operator. There are no significant differences between these top performing results, which includes the 2D 15x15 and 21x21 Median, 3D Median with depths of 3, 5, 11, and 21, and 2D Gaussian with variances of 9, 16, and 25.

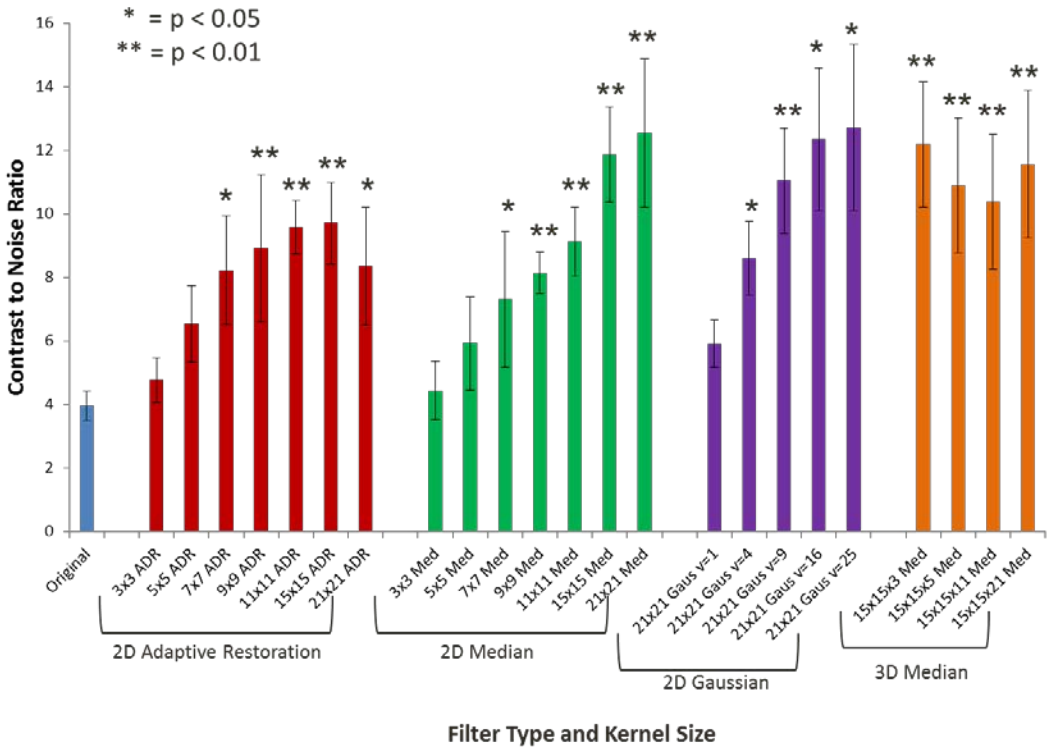

Figure 11. Mean CNR of various 2D and 3D filter types and kernel sizes.

Table 6. Mean CNR of various 2D and 3D filter types and kernel sizes.

	Raw	3 ADR	5 ADR	7 ADR	9 ADR	11 ADR	15 ADR	21 ADR	3 Med	5 Med	7 Med	9 Med
1086_1	3.95	4.77	6.53	8.23	8.91	9.58	9.70	8.36	4.44	5.93	7.31	8.14
1089_4	3.56	4.49	5.65	7.08	8.44	9.52	11.17	11.06	4.49	5.77	7.37	8.99
2710_1	5.52	3.91	4.95	5.65	5.76	5.19	3.96	2.44	3.78	4.69	5.524	6.17
2712_1	6.64	0.58	0.53	0.82	1.80	2.24	1.03	-3.24	0.67	0.84	1.17	2.06
1087_2	3.32	6.83	8.62	10.60	12.62	14.46	16.93	16.24	6.54	8.16	10.19	12.19
1088_4	1.69	7.33	9.88	13.53	17.49	20.52	24.083	22.52	6.94	9.08	12.03	14.98
1090_3	5.66	6.72	8.49	10.35	11.77	12.78	13.853	13.42	6.52	8.16	9.956	11.52
1087_3	5.72	8.142	10.60	13.33	15.42	16.77	17.67	15.11	7.89	10.06	12.67	14.86
1088_1	5.21	6.482	8.64	11.13	13.20	14.70	15.86	14.91	6.28	8.25	10.61	12.92
1089_1	4.96	6.04	7.87	10.02	11.77	12.69	12.47	10.83	5.85	7.52	9.72	11.87
Mean	4.62	5.532	7.17	9.07	10.72	11.85	12.67	11.17	5.34	6.85	8.65	10.37
Std Dev	1.47	2.19	2.93	3.82	4.62	5.41	6.73	7.31	2.07	2.66	3.43	4.06
Std Error	0.46	0.692	0.93	1.21	1.46	1.71	2.13	2.31	0.65	0.84	1.08	1.28
Ttest		0.38	**0.063**	**0.015**	**0.0070**	**0.0059**	**0.0096**	**0.036**	0.46	0.078	**0.017**	**0.005**
	11 Med	**15 Med**	**21 Med**	**Gaus v=1**	**Gaus v=4**	**Gaus v=9**	**Gaus v=16**	**Gaus v=25**	**15x3 Med**	**15x5 Med**	**15x11 Med**	**15x21 Med**
1086_1	9.13	11.86	12.53	5.10	7.58	9.13	9.85	9.74	12.18	10.89	10.37	11.56
1089_4	10.16	11.76	13.89	4.84	6.75	8.70	10.37	11.66	12.04	11.40	10.70	10.41
2710_1	6.56	6.13	4.86	4.15	5.54	4.97	3.59	2.67	5.96	6.84	7.69	7.54
2712_1	2.47	3.16	-0.14	0.62	0.56	1.06	-0.78	-3.02	2.54	1.08	1.15	0.82
1087_2	14.01	17.688	17.81	7.22	10.19	13.37	16.07	17.64	18.82	18.55	18.78	21.19
1088_4	17.84	22.59	26.49	7.83	12.57	18.69	23.85	26.56	22.87	23.57	21.76	23.33
1090_3	12.85	14.414	14.50	7.17	9.98	12.23	13.55	14.13	14.06	14.04	14.14	14.48
1087_3	16.62	19.12	19.21	8.71	12.71	16.16	17.60	17.51	19.78	20.55	22.23	23.60
1088_1	14.88	16.75	14.66	6.99	10.54	13.95	16.03	16.75	17.38	17.63	18.39	18.49
1089_1	13.22	13.41	11.07	6.48	9.45	12.10	13.31	13.37	13.69	14.99	15.84	15.82
Mean	11.77	13.698	13.49	5.91	8.59	11.04	12.34	12.70	13.93	13.96	14.10	14.72
Std Dev	4.73	5.86	7.37	2.34	3.65	5.23	7.06	8.27	6.24	6.70	6.68	7.33
Std Error	1.49	1.85	2.33	0.74	1.15	1.66	2.23	2.61	1.97	2.11	2.11	2.31
Ttest	**0.003**	**0.0024**	**0.0093**	0.24	**0.021**	**0.0094**	**0.014**	**0.023**	**0.0028**	**0.0038**	**0.0031**	**0.0036**

The Sobel operator is a differential operator used to compute the gradient of the image intensity function[10]. Gradients are found in the x and y direction using kernels such as the 5x5 kernels shown in Figure 12. The absolute magnitude of the gradient and direction of edges can be determined by combining measurements obtained after applying both kernels. The edge strength from the Sobel results were calculated in the same way as the

CNR from the low-pass filtered images, with ROIs manually placed on the abdominal wall edge and the surrounding tissue, as in Figure 13.

$$S_x = \begin{bmatrix} 1 & 2 & 0 & -2 & -1 \\ 4 & 8 & 0 & -8 & -4 \\ 6 & 12 & 0 & -12 & -6 \\ 4 & 8 & 0 & -8 & -4 \\ 1 & 2 & 0 & -2 & -1 \end{bmatrix} \quad S_y = \begin{bmatrix} -1 & -4 & -6 & -4 & -1 \\ -2 & -8 & -12 & -8 & -2 \\ 0 & 0 & 0 & 0 & 0 \\ 2 & 8 & 12 & 8 & 2 \\ 1 & 4 & 6 & 4 & 1 \end{bmatrix}$$

Figure 12. 5x5 Sobel kernels for x and y gradient direction[12].

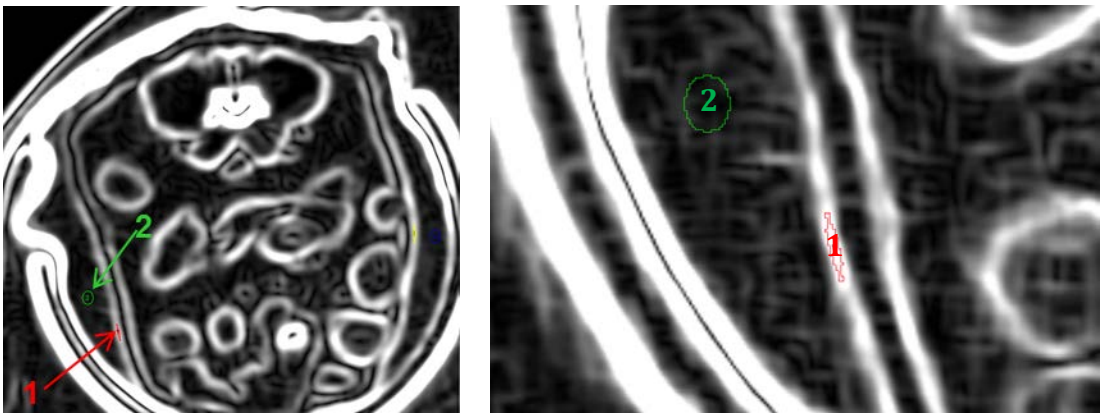

Figure 13. ROI placement on the abdominal edge and surrounding tissue for edge strength measurement.

A median filtered image is shown in Figure 14a, with the Sobel operator results performed on the raw CT image using a 5x5 kernel displayed in Figure 14b. The Sobel operator on the raw image seems to capture the edges from the CT gantry and outer boundary of the mouse, with the abdominal wall edges of interest hidden within the image noise. Increased Sobel kernel size thickens the edges when applied to low-pass filtered images, but also makes these abdominal wall lines more continuous. Noise from the background also seems to be reduced at increased kernel sizes.

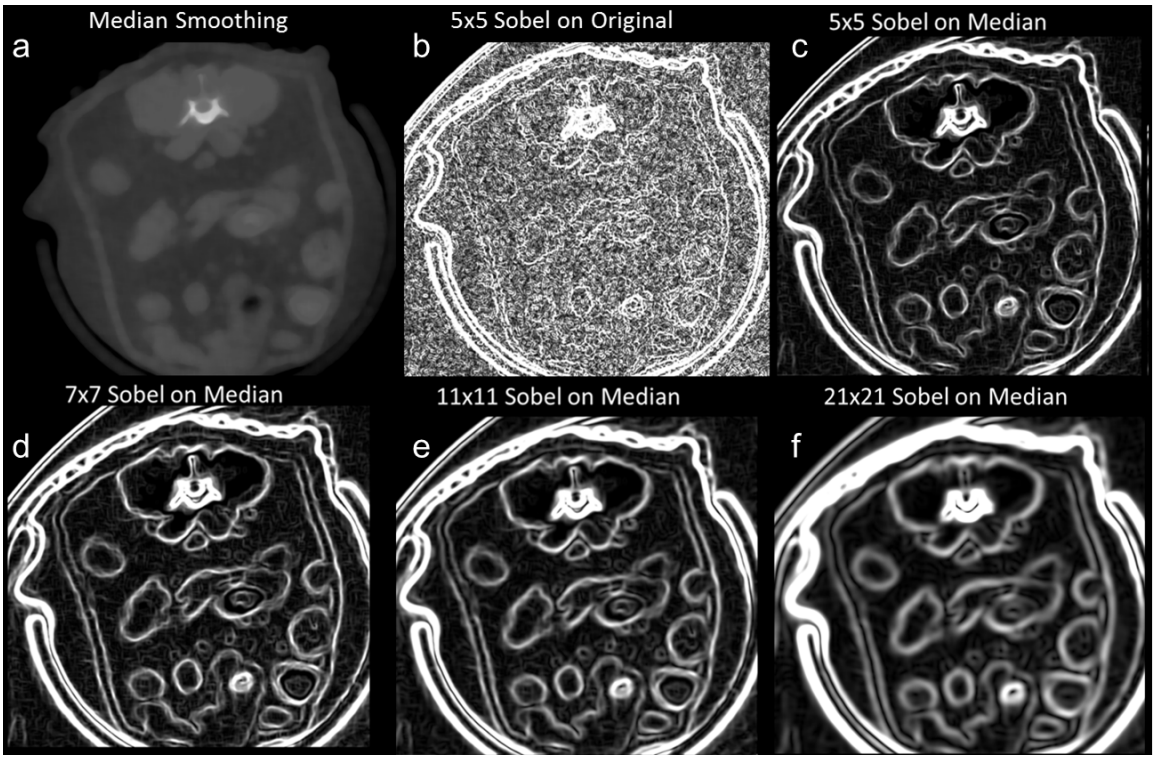

Figure 14. a) Median filter applied onto a raw CT volume, b) 5x5 Sobel operator applied onto raw CT volume and Sobel operator of sizes c) 5x5, d) 7x7, e) 11x11, and f) 21x21 applied onto 3D 15x15x3 Median filtered volumes.

The Sobel operator was performed using kernel sizes of 5x5, 7x7, 11x11, and 21x21 on the 2D 15x15 and 21x21 Median, 3D Median with depths of 3, 5, 11, and 21, and 2D Gaussian at variances of 9, 16 and 25. Statistical results seem to be similar across the low-pass filtered results. Edge detection does seem to perform better with increased Sobel kernel sizes, such as with the 11x11 and 21x21 Sobel kernels. The quantitative performance of the various Sobel kernel sizes performed across different low-pass filtering methods can be seen in Table 7.

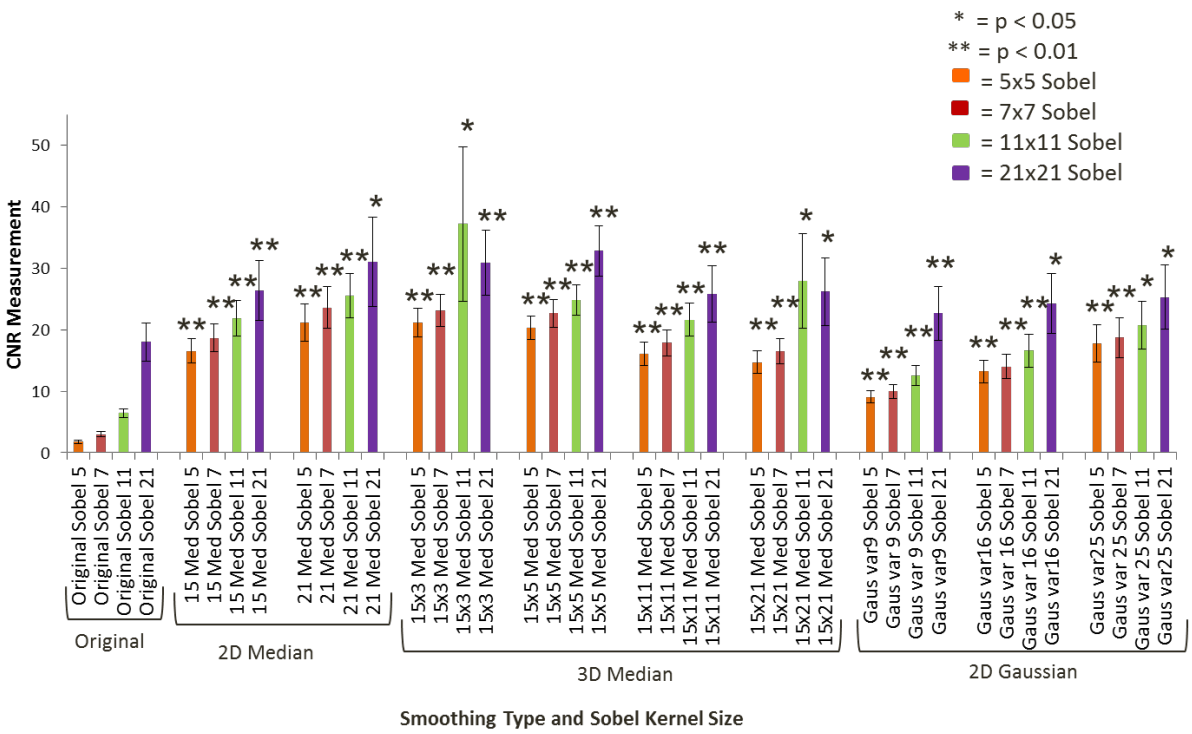

Figure 15. Edge strength of various unsmoothed and smoothed volumes after Sobel operator application of various kernel sizes.

Table 7. Edge strength for individual mice for various unsmoothed and smoothed volumes after Sobel operators of various kernel sizes.

	Raw Sobel 5	Raw Sobel 7	Raw Sobel 11	Raw Sobel 21	15 Med Sobel 5	15 Med Sobel 7	15 Med Sobel 11	15 Med Sobel 21	21 Med Sobel 5	21 Med Sobel 7	21 Med Sobel 11	21 Med Sobel 21	15x3 Med Sobel 5	15x3 Med Sobel 7	15x3 Med Sobel 11	15x3 Med Sobel 21	15x5 Med Sobel 5	15x5 Med Sobel 7	15x5 Med Sobel 11	15x5 Med Sobel 21
1086_1	1.21	1.62	3.32	6.83	3.39	4.52	5.86	8.90	3.19	4.16	6.11	8.69	5.26	6.82	9.20	10.66	5.72	7.16	9.28	11.88
1089_4	1.10	1.26	2.72	12.58	4.35	5.57	8.74	11.72	1.89	2.19	3.31	9.66	5.30	6.11	7.53	12.11	4.46	5.64	7.52	12.12
2710_1	1.80	2.51	4.49	12.78	3.57	4.73	5.83	11.56	2.58	3.02	3.99	10.1	3.65	4.74	5.93	11.37	3.14	3.96	5.92	10.91
2712_1	1.67	2.29	3.66	4.02	4.08	5.14	5.55	4.84	5.71	6.93	6.40	5.67	4.58	6.43	7.46	7.42	3.49	4.55	6.04	5.10
1087_2	1.40	2.06	5.37	11.36	2.63	3.64	6.42	7.62	3.53	4.33	4.54	6.41	3.22	4.32	7.67	9.83	4.03	5.60	8.94	13.49
1088_4	1.88	2.55	4.61	10.19	4.61	5.52	6.97	11.12	3.13	4.02	7.66	14.71	5.49	6.45	7.99	13.80	3.98	4.37	5.28	10.23
1090_3	1.22	1.48	2.37	5.43	3.33	3.36	3.55	4.58	3.00	3.09	3.69	4.77	3.78	4.42	5.20	5.69	4.36	4.89	5.30	5.46
1087_3	2.32	3.40	5.67	4.82	3.26	3.91	5.67	4.16	3.24	3.73	5.16	4.52	4.06	4.75	12.87	6.54	3.11	3.59	17.74	6.85
1088_1	1.58	2.17	3.63	9.03	3.13	3.74	6.00	6.79	3.71	4.10	4.25	5.46	4.73	5.94	8.30	9.22	4.21	4.66	6.78	9.17
1089_1	1.71	2.18	4.19	6.09	3.40	3.93	5.67	5.77	3.76	4.58	5.74	3.99	3.16	4.20	6.50	8.67	3.10	4.13	6.20	7.41
Mean	1.59	2.15	4.00	8.31	3.57	4.41	6.02	7.71	3.37	4.01	5.08	7.41	4.32	5.42	7.86	9.53	3.96	4.85	7.90	9.26
Std Dev	0.37	0.61	1.07	3.29	0.60	0.80	1.29	2.96	0.99	1.25	1.38	3.37	0.87	1.02	2.11	2.55	0.81	1.04	3.72	2.93
Std Error	0.11	0.19	0.33	1.04	0.19	0.25	0.41	0.94	0.31	0.39	0.43	1.06	0.27	0.32	0.66	0.80	0.26	0.32	1.17	0.92
Ttest					**8.52E-06**	**3.67E-06**	**3.35E-06**	**0.000145**	**0.00026**	**0.000143**	**1.17E-05**	**0.000434**	**1.3E-05**	**2.42E-06**	**2.92E-06**	**5.21E-06**	**8.45E-05**	**3.3E-05**	**0.000331**	**2.53E-05**

	15x11 Med Sobel 5	15x11 Med Sobel 7	15x11 Med Sobel 11	15x11 Med Sobel 21	15x21 Med Sobel 5	15x21 Med Sobel 7	15x21 Med Sobel 11	15x21 Med Sobel 21	Gaus var9 Sobel 5	Gaus var 9 Sobel 7	Gaus var 9 Sobel 11	Gaus var9 Sobel 21	Gaus var16 Sobel 5	Gaus var16 Sobel 7	Gaus var16 Sobel 11	Gaus var16 Sobel 21	Gaus var25 Sobel 5	Gaus var25 Sobel 7	Gaus var25 Sobel 11	Gaus var25 Sobel 21
1086_1	5.80	5.74	5.50	9.20	3.59	3.93	4.55	8.46	4.49	4.94	6.27	7.91	6.55	6.79	7.41	8.81	7.32	7.38	7.71	10.83
1089_4	3.19	3.70	5.50	7.74	2.84	3.41	4.47	6.02	3.22	3.72	6.26	10.56	6.56	7.39	9.44	9.28	12.25	11.88	11.36	8.30
2710_1	4.27	4.46	6.22	10.64	2.10	2.46	8.36	12.46	5.10	5.39	6.85	9.96	7.52	7.90	8.98	8.33	10.06	9.93	10.07	7.37
2712_1	2.53	2.98	3.69	4.61	2.65	3.36	8.38	5.12	4.21	4.34	4.58	4.00	4.64	4.47	4.16	4.35	4.52	4.22	3.97	5.23
1087_2	2.91	3.68	4.77	6.65	2.46	2.76	3.67	5.90	6.98	7.30	8.66	7.90	10.98	11.28	12.22	7.68	13.07	11.74	9.38	8.02
1088_4	2.29	2.60	3.56	9.43	2.16	2.33	2.98	9.05	6.16	6.72	8.30	10.18	9.17	9.32	10.32	10.02	11.44	11.30	11.51	10.64
1090_3	2.41	2.81	3.89	9.92	2.39	2.57	3.10	4.55	3.12	3.36	4.17	5.40	4.57	4.65	5.04	5.32	5.63	5.42	5.40	5.50
1087_3	3.01	3.19	3.86	6.39	3.98	3.37	3.37	7.19	7.90	7.73	7.19	4.46	7.70	7.07	6.18	4.78	5.73	5.32	4.72	4.37
1088_1	3.64	3.81	5.33	7.96	2.73	3.27	5.14	7.52	5.48	6.22	8.40	6.51	8.96	8.86	9.42	5.98	9.74	9.87	7.83	6.47
1089_1	3.16	4.02	5.92	5.52	3.48	4.12	5.78	3.65	6.07	6.38	7.19	5.76	7.71	7.51	6.93	6.42	6.56	6.22	5.62	7.83
Mean	3.32	3.70	4.83	7.81	2.84	3.16	4.98	6.99	5.27	5.61	6.79	7.26	7.44	7.52	8.01	7.10	8.63	8.33	7.76	7.46
Std Dev	1.05	0.92	1.00	1.99	0.63	0.61	1.99	2.56	1.55	1.50	1.52	2.40	1.99	2.04	2.50	1.99	3.05	2.93	2.76	2.15
Std Error	0.33	0.29	0.31	0.63	0.20	0.19	0.63	0.81	0.49	0.47	0.48	0.76	0.62	0.64	0.79	0.63	0.96	0.92	0.87	0.68
Ttest	**0.0013**	**0.00018**	**1.04E-05**	**6.55E-06**	**0.00020**	**9.43E-05**	**0.000449**	**7.41E-05**	**8.99E-06**	**3.51E-06**	**1.24E-06**	**5.96E-05**	**5.12E-06**	**7.09E-06**	**2.54E-05**	**1.93E-05**	**6.22E-05**	**6.52E-05**	**8.18E-05**	**2.19E-05**

The effects of the 5x5 and 21x21 Sobel operator on the various filter types and sizes are displayed in Figure 16 for comparison with the effects on the original, unsmoothed image. The smoothing steps helped create more continuous abdominal wall edges and less image noise as opposed to the original CT volume.

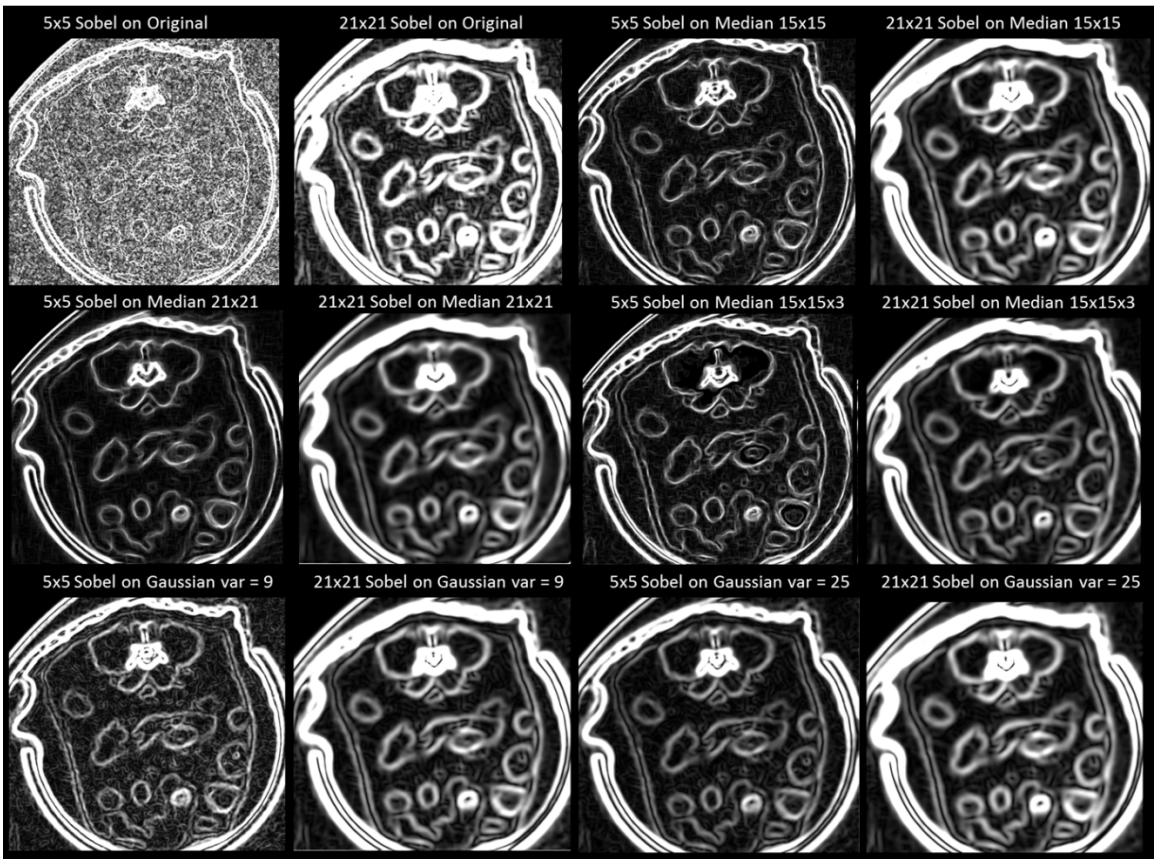

Figure 16. Sobel operator results using kernel sizes of 5x5 versus 21x21 on raw CT, 2D Median 15x15 and 21x21, 3D Median 15x15x3, and Gaussian smoothed volumes of variances 9 and 25.

Discussion

As stated previously, 2D low-pass filtering results demonstrate improved CNR for ADR and median kernels of 7x7 and greater, and at Gaussian variances of 4 and higher. At larger kernel sizes for the ADR filter, it can be observed that the outer boundary values are not preserved fully, such as in Figure 6. This affects lean mice more significantly, as these mice have lower amounts of fat throughout their bodies, including subcutaneous fat. Therefore, the abdominal wall was affected in lean mice, such as mouse 2712_1, at larger kernel sizes, as can be observed in a negative CNR found in Table 2 at the 21x21 kernel size. This could have resulted due to a partial-volume effect whereby non-abdominal wall

tissue was averaged into the abdominal wall region for the ROI analysis. The same phenomena was also observed for the largest 2D median kernel size of 21x21 and the 2D Gaussian with variance of 25 on the same lean mouse (2712_1). This could be due to the fact that mouse 2712_1 is the leanest mouse within the sample, weighing at 19.96 g. With so little fat, it is difficult to discriminate between the outer skin boundary and abdominal wall, or even find a fat tissue region for the ROI calculation. The 2D 15x15 and 21x21 median, 3D median with depths of 3, 5, 11 and 21, and Gaussian filters of variances 9,16, and 25 were chosen to be evaluated for the Sobel operator based on both the CNR results and general image appearance. Higher Sobel kernel sizes demonstrated better results, with the 11x11 and 21x21 kernel sizes resulting in thicker, more continuous edges along the abdominal wall. The next steps for the remainder of my time at Genentech will be to complete the Canny steps with non-maximum suppression, double thresholding and edge tracking by hysteresis. In addition to completing the remainder of the 5 Canny steps, my future steps include the application of morphological filtering to segment out the visceral and subcutaneous fat compartments. In addition, the start and stop slice selection would be automated in order to fully automate the algorithm.

Conclusion

This study aimed to develop methods to aid edge detection for the proper segmentation of visceral and subcutaneous fat from micro-CT volumes. The median and Gaussian smoothed images showed the greatest promise when used in conjunction with larger Sobel kernel sizes. Future applications of this algorithm would be to automatically assess fat depots for use in longitudinal studies of adipose development, as central obesity is associated with increased risk for diabetes, hypertension and heart disease.

References

1. Tchkonia et al. Mechanism and Metabolic Implications of Regional Differences among Fat Depots. Cell Metabolism, Vol 17, 2013.
2. Horvat et al. Comparison of anthropometric, area- and volume-based assessment of abdominal subcutaneous and visceral adipose tissue volumes using multi-detector computed tomography. International Journal of Obesity, Vol 31, 2006.
3. Luu et al. In vivo quantification of subcutaneous and visceral adiposity by micro-computed tomography in a small animal model. Medical Engineering & Physics, Vol 31, 2009.
4. Miesel et al. Overfeeding-Induced Obesity in Spontaneously Hypertensive Rats: An Animal Model of the Human Metabolic Syndrome. Annals of Nutrition & Metabolism, Vol 56, 2010.
5. Lublinsky et al. Automated Separation of Visceral and Subcutaneous Adiposity in In Vivo Microcomputed Tomographies of Mice. Journal of Digital Imaging, Vol 22, 2009.
6. Kim et al. Body Fat Assessment Method Using CT Images with Separation Mask Algorithm. Journal of Digital Imaging, Vol 26, 2012, pp 155-162.
7. Chung et al. Automated Segmentation of Muscle and Adipose Tissue on CT images for Human Body Composition Analysis. Medical Imaging 2009.
8. Wyatt et al. Unpublished work.
9. Canny. A Computational Approach to Edge Detection. IEEE Transactions on Pattern Analysis and Machine Intelligence. Vol 6, 1986.
10. “Canny Edge Detection.” <http://www.cse.iitd.ernet.in/~pkalra/csl783/canny.pdf>

11. Analyze Direct. <http://www.analyzedirect.com/support/resourcecenter.asp>.
12. Pratt. Digital Image Processing. Wiley-Interscience Publication, 1991. pp 294-295.
13. “5x5 Sobel Kernel Image” <http://openi.nlm.nih.gov/imgs/rescaled512/3224570_1471-2105-11-558-9.png>

Publishing Agreement

It is the policy of the University to encourage the distribution of all theses, dissertations, and manuscripts. Copies of all UCSF theses, dissertations, and manuscripts will be routed to the library via the Graduate Division. The library will make all theses, dissertations, and manuscripts accessible to the public and will preserve these to the best of their abilities, in perpetuity.

Please sign the following statement:

I hereby grant permission to the Graduate Division of the University of California, San Francisco to release copies of my thesis, dissertation, or manuscript to the Campus Library to provide access and preservation, in whole or in part, in perpetuity.

Charvi Shetty
Author Signature

9/9/13
Date